Rock and Soil Mechanics

Volume 44 | Issue 6 Article 5

10-3-2023

# Improvement of rainfall boundary treatment based on the diffusion wave approximation equation

Xu WANG
*Research Center of Coastal and Urban Geotechnical Engineering, Zhejiang University, Hangzhou, Zhejiang 310058, China*, wangxu0803@zju.edu.cn

Mei DONG
*Research Center of Coastal and Urban Geotechnical Engineering, Zhejiang University, Hangzhou, Zhejiang 310058, China*

Meng-yue KONG
*Hangzhou Archaeological Ruins of Liangzhu City World Heritage Monitoring and Management Center, Hangzhou, Zhejiang 311113, China*

Yun-peng DENG
*Research Center of Coastal and Urban Geotechnical Engineering, Zhejiang University, Hangzhou, Zhejiang 310058, China*

*See next page for additional authors*

# Improvement of rainfall boundary treatment based on the diffusion wave approximation equation


## Authors

Xu WANG, Mei DONG, Meng-yue KONG, Yun-peng DENG, Ri-qing XU, and Xiao-nan GONG

Rock and Soil Mechanics 2023 44(6): 1761−1770 ISSN 1000−7598
https: //doi.org/10.16285/j.rsm.2022.6104 http://rocksoilmech.researchcommons.org/journal

# Improvement of rainfall boundary treatment based on the diffusion wave approximation equation

WANG Xu[1], DONG Mei[1], KONG Meng-yue[2], DENG Yun-peng[1], XU Ri-qing[1], GONG Xiao-nan[1]
1. Research Center of Coastal and Urban Geotechnical Engineering, Zhejiang University, Hangzhou, Zhejiang 310058, China
2. Hangzhou Archaeological Ruins of Liangzhu City World Heritage Monitoring and Management Center, Hangzhou, Zhejiang 311113, China

**Abstract:** During the simulation of rainwater infiltration, the conventional rainfall boundary cannot accurately reflect the influence of the variation of ponding water depth on the calculation of actual rainwater infiltration rate. To address this issue, the conventional rainfall boundary is improved by incorporating the diffusion wave approximation equation, allowing for the coupling of ponding water depth variations with actual infiltration rate during heavy rainfall events. Additionally, the accuracy of the improved boundary is validated through two classical experimental cases. The improved boundary is subsequently applied to the simulation of an actual engineering scenario. The findings indicate that the improved rainfall boundary is capable of achieving real-time dynamic transition between flux and pressure head boundaries. When the rainfall boundary functions as the pressure head boundary, the theoretical maximum ponding water depth calculated by the improved boundary is located at the slope toe. Conversely, when the rainfall boundary serves as the flux boundary during the final stage of rainfall, the ponding water depth becomes negligible, and the theoretical maximum ponding water depth is located at the intersection of the flat and steep slope surface.

**Keywords:** rainfall boundary; seepage; diffusion wave approximation equation; real-time dynamic transition

## 1 Introduction

Slope instability is a severe natural disaster, and research has shown that it is closely related to the rainfall process[1]. In the seepage calculation and stability analysis of soil slopes under heavy rainfall conditions, the treatment of rainfall boundaries directly affects the accuracy of the analysis results[2].

To simplify the simulation of rainwater infiltration patterns under heavy rainfall conditions, some studies treated the rainfall boundary as a flux boundary. In this approach, the infiltration rate is directly specified or reduced based on empirical values[3]. Although this method provides some simplification, it overlooks the crucial process of converting the boundary condition from a flux boundary to a pressure head boundary, resulting in significant inaccuracies. In more complex rainfall conditions, the actual treatment of the rainfall boundary involves the mutual transition between flux and pressure head boundaries[4]. Considerable research progress has been made in this area. For instance, Lou[5] conducted the transient analysis of the slope seepage field under rainfall conditions using finite element methods, and suggested that when the rainfall intensity exceeds the infiltration capacity of the soil, a portion of the rainfall will infiltrate into the soil, while the remainder will form surface runoff, leading to the transition of the rainfall boundary into a pressure head boundary. May et al.[6] implemented the simulation of complex rainfall by combining Cauchy boundary condition with a complementary smooth function. Nian et al.[4] used pore water pressure as a control variable, and deduced the governing equations for two types of rainwater infiltration boundaries, thereby addressing the problem of determining the maximum infiltration capacity. Hou et al.[7] implemented the simulation of rainwater infiltration into fractured soil by using air units. Dou et al.[8] used the difference between rainfall recharge and actual infiltration as the criterion for dynamic switching between two types of rainfall boundaries, allowing for real-time, bi-directional transition between flux and pressure head boundaries.

Although there has been significant advancement in the rainfall boundary research in recent years, some limitations still exist. For instance, the aforementioned studies generally assumed that the pressure head of the soil surface remains constant when the slope surface becomes saturated, and the determination of the soil surface pressure is often based on the empirical methods. However, this assumption lacks accuracy since the ponding water depth on the slope surface undergoes dynamic changes under intense rainfall conditions. Furthermore, studies have indicated that the variation in ponding water depth on the slope surface plays a crucial role in the stability of shallow slopes and rainwater infiltration rate[9].

Received: 15 July 2022 Accepted: 21 October 2022
This work was supported by the Key Research & Development Program of Zhejiang Province (2022C03180) and the Zhejiang Provincial Project for Science and Technology in the Protection of Cultural Heritage (2021021).
First author: WANG Xu, male, born in 1997, Master degree candidate, majoring in slope stability analysis. E-mail: wangxu0803@zju.edu.cn

Therefore, based on the existing research, this study introduces the diffusion wave approximation equation to describe the dynamic change in runoff depth on the slope surface. This serves as an improvement to the conventional governing equations used for rainfall boundaries. The accuracy of the improved rainfall boundary is validated through the utilization of two well-known experimental cases, i.e. the Lima model test[10] and the Abdul model test[11]. Additionally, the study applies the improved boundary to analyze the development patterns of surface runoff and the infiltration characteristics of rainfall on the slope of an earthen archaeological site under concentrated rainfall conditions.

## 2 Primary governing equations

### 2.1 Richard's equation

The classical equations utilized in the description of unsaturated groundwater seepage include the Richard's equation and the two-phase flow equation. Due to the advantages of the Richard's equation, i.e. its straightforward form and the clear physical meaning of the parameters, we have opted to employ the Richard's equation in this study to depict the variably saturated flow within the soil:

$$\rho\left(\frac{C}{\rho g}+S_{\mathrm{e}}S_0\right)\frac{\partial p}{\partial t}-\nabla\cdot\rho\left[\frac{K_{\mathrm{s}}k_{\mathrm{r}}}{\rho g}(\nabla p+\rho g\nabla D)\right]=Q_{\mathrm{w}} \quad (1)$$

where $\nabla$ is the vector differential operator; $p$ is the pore water pressure (kPa); $C$ is the specific moisture capacity ($m^{-1}$); $S_e$ is the effective degree of saturation; $K_s$ is the saturated coefficient of permeability ($m \cdot s^{-1}$); $k_r$ is the relative hydraulic conductivity; $\rho$ is the water density ($kg \cdot m^{-3}$); $g$ is the gravitational acceleration ($m \cdot s^{-2}$); $Q_w$ is the source-sink term of water ($kg \cdot m^{-3} \cdot s^{-1}$); $D$ is the position in Cartesian coordinates system (m); and $S_0$ is the specific storage coefficient ($kg^{-1} \cdot m \cdot s^2$).

The storage coefficient $S_0$ can be expressed as follows[4]:

$$S_0=n_0\chi_{\mathrm{f}}+\chi_{\mathrm{p}} \quad (2)$$

where $n_0$ is the porosity of soil; $\chi_f$ is the coefficient of compressibility for the water ($kg^{-1} \cdot m \cdot s^2$); and $\chi_p$ is the coefficient of effective compressibility of soil skeleton ($kg^{-1} \cdot m \cdot s^2$).

The soil−water characteristic curve model proposed by Van Genuchten[13], known as the Van Genuchten (VG) model, can be used to describe the relationships between various parameters in the unsaturated soil:

$$\theta=\begin{cases}\theta_{\mathrm{r}}+\dfrac{\theta_{\mathrm{s}}-\theta_{\mathrm{r}}}{\left[1+\left(\alpha h_0\right)^n\right]^m}, h_0<0\\ \theta_{\mathrm{s}}, h_0\geqslant 0\end{cases} \quad (3)$$

$$S_{\mathrm{e}}=\begin{cases}\left(1+\left|\alpha h_0\right|^n\right)^{-m}, h_0<0\\ 1, h_0\geqslant 0\end{cases} \quad (4)$$

$$k_{\mathrm{r}}=\begin{cases}S_{\mathrm{e}}^{0.5}\left[\left(1-(1-S_{\mathrm{e}}^{\frac{1}{m}})\right)^m\right]^2, h_0<0\\ 1, h_0\geqslant 0\end{cases} \quad (5)$$

$$C=\begin{cases}\dfrac{\alpha m}{1-m}(\theta_{\mathrm{s}}-\theta_{\mathrm{r}})S_{\mathrm{e}}^{\frac{1}{m}}(1-S_{\mathrm{e}}^{\frac{1}{m}})^m, h_0<0\\ 0, h_0\geqslant 0\end{cases} \quad (6)$$

where $\theta$ is the volumetric water content; $\theta_s$ and $\theta_r$ are the saturated and residual volumetric water contents, respectively; $h_0$ is the pore water pressure head (m); and $\alpha$, $n$, $m$ and $l$ are the constants, where Mualem[18] suggested that $m = 1 - 1/n$.

### 2.2 Diffusion wave approximation equation

The diffusion wave approximation equation has been widely used to characterize the dynamics of surface runoff on the slopes[12, 15], particularly the variation in ponding water depth on the slope surface. Since the water depth of surface runoff is extremely shallow, the vertical ponding water depth on the slope surface can be approximated as the vertical distance between the water surface and the slope surface[15]. Consequently, the mass conservation equation for the surface runoff can be expressed as follows:

$$\frac{\partial h}{\partial t}+\nabla\cdot(h\vec{u})=R-I \quad (7)$$

where $t$ is the time (s); $h$ is the vertical ponding water depth (m); $\vec{u}$ represents the average flow velocity in the depth direction (m /s); $R$ is the rainfall intensity (m /s); and $I$ is the infiltration rate (m /s).

Considering the balance between the friction term and the driving force term in the momentum conservation equation, and combined with the Manning formula[16], the following expression can be obtained:

$$\vec{u}=-\frac{h^{\frac{2}{3}}}{n_{\mathrm{m}}\sqrt{|S|}}\nabla(h+z_{\mathrm{f}}) \quad (8)$$

where $n_m$ is the Manning's friction coefficient ($s/m^{1/3}$); $z_f$ is the elevation of the slope surface (m); $S$ is the slope ratio, where $S = \nabla z_f$; and $q$ is the flow rate of surface runoff on the slope ($m^2/s$), which can be expressed as the product of runoff velocity and water head:

$$q=h\vec{u}=-\frac{h^{\frac{5}{3}}}{n_{\mathrm{m}}\sqrt{|S|}}\nabla(h+z_{\mathrm{f}}) \quad (9)$$

By substituting Eq. (9) into Eq. (7), the diffusion wave approximation equation can be obtained as follows:

$$\frac{\partial h}{\partial t}-\nabla\cdot\left[\frac{h^{\frac{5}{3}}}{n_{\mathrm{m}}\sqrt{|S|}}\nabla(z_{\mathrm{f}}+h)\right]=R-I \tag{10}$$

## 3 Improved treatment of rainfall boundary

### 3.1 Conventional treatment of rainfall boundary

In the numerical simulations, the modeling of rainfall boundary often necessitates a dynamic transition between pressure head and flux boundaries[4, 6]. Conventionally, it is assumed that when the soil surface is unsaturated, the actual rainwater infiltration rate is equal to the rainfall intensity, thereby a flux boundary is adopted. As saturation is reached on the slope surface, rainfall can be divided into two components: a fraction infiltrates into the soil, while the rest accumulates on the surface and forms the surface runoff. The actual infiltration rate on the slope surface is governed by the dynamically varying depth of runoff, and thus the rainfall boundary transitions into a time-dependent pressure head boundary. When the rainfall boundary is treated as a pressure head boundary, the permeability characteristics of the slope surface resemble a semi-permeable layer. The model domain integrates surface ponding water through this semi-permeable layer (Fig. 1), and the infiltration rate is influenced by the water head difference across the semi-permeable layer and its hydraulic conductivity[4]. Hence, when the soil surface is unsaturated, the infiltration rate can be expressed as follows:

$$I=R \tag{11}$$

When the soil surface is saturated, the infiltration rate can be expressed as

$$I=R_{\mathrm{b}}\left(H_{\mathrm{b}}-H\right) \tag{12}$$

where $R_{\mathrm{b}}$ is the conductivity of the semi-permeable layer to the fluid under the action of water head difference ($\mathrm{m}^{-1}$); $H_{\mathrm{b}}$ is the water head of the fluid source outside the semipermeable layer (m); and $H$ is the water head of the model domain in the semi-permeable layer (m).

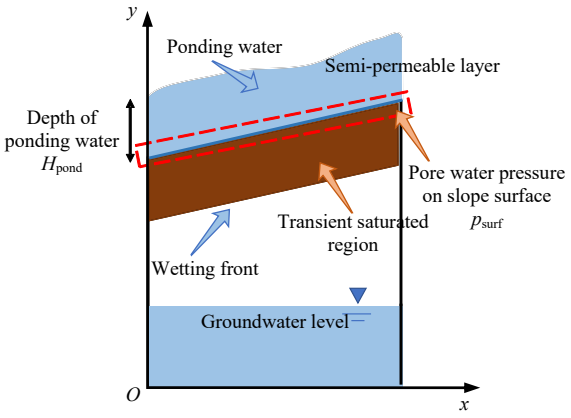


**Fig. 1 Schematic diagram of ponding water infiltration**

$R_{\mathrm{b}}$ can be determined by solving the following equation[4, 8]:

$$R_{\mathrm{b}}=\frac{K_{\mathrm{s}}}{L} \tag{13}$$

where $L$ is the thickness of the semi-permeable layer (m), which is an equivalent physical quantity that cannot be directly measured and its specific value can be referred to Nian et al.[4].

Figure 1 is taken as an example. By substituting the water head values at the upper and lower ends of the semi-permeable layer into Eq. (12), the infiltration rate of the soil surface under the pressure head boundary can be obtained as follows:

$$I=\frac{K_{\mathrm{s}}}{L}\left(H_{\mathrm{pond}}-\frac{p_{\mathrm{surf}}}{\rho g}\right) \tag{14}$$

where $H_{\mathrm{pond}}$ is the ponding water depth on the slope surface (m); and $p_{\mathrm{surf}}$ is the pore water pressure (kPa).

This study utilizes the pore water pressure on the slope surface as the controlling variable for the mutual transition of boundary condition. If the pressure on the surface is below 0, it indicates unsaturation, while a value above 0 indicates saturation of the slope surface. To avoid numerical instabilities due to abrupt changes during the boundary condition transition, the step smoothing functions are employed to integrate the pressure head and flux boundaries. The expression for the rainfall boundary is

$$I=\alpha(p_{\mathrm{surf}})R+\beta(p_{\mathrm{surf}})\frac{K_{\mathrm{s}}}{L}\left(H_{\mathrm{pond}}-\frac{p_{\mathrm{surf}}}{\rho g}\right) \tag{15}$$

where $\alpha(p)$ and $\beta(p)$ are the step smoothing functions (Fig. 2).

When the conventional rainfall boundary is used to treat the rainwater infiltration on a slope surface, it is commonly assumed that the ponding water depth in Eq. (15) remains constant[4, 6–8]. However, in reality, the ponding water depth during rainwater infiltration varies dynamically rather than remaining constant. This means that the assumption made by conventional rainfall boundary leads to a fixed water head difference across the pressure head boundary when the slope reaches saturation. This limitation makes it impossible to achieve the reverse transition from the pressure head boundary to the flux boundary during the final stage, regardless of any changes in rainfall intensity. Consequently, this assumption introduces a certain degree of computational error[8].

### 3.2 Improved algorithm for rainfall boundary based on diffusion wave approximation equation

This research utilizes the finite element software COMSOL Multiphysics, which supports the multiple physics coupling. Considering the limitations of the

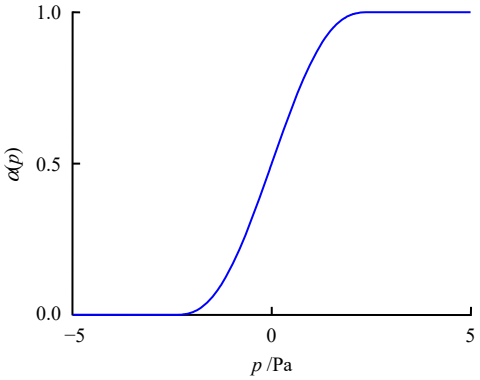


(a) Relationship between $\alpha$ and $p$

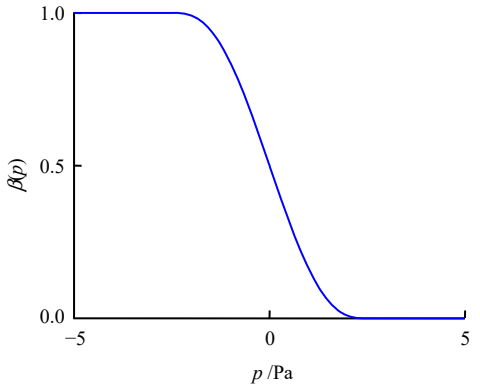


(b) Relationship between $\beta$ and $p$

**Fig. 2 Step smoothing functions**

aforementioned rainfall boundary governing equation, based on the conventional rainfall boundary model, the nodal pore pressure is used as the determinant of soil surface saturation. Following this, a diffusion wave approximation equation, facilitated by the user-defined partial differential equations (PDE) module in COMSOL, is then incorporated to depict the variation in ponding water depth on the slope. The calculated ponding water depth for each time increment is input in Eq. (15) to determine the infiltration rate at the soil surface. Subsequently, the Richard's equation for that particular time increment is solved. Through the improved rainfall boundary, the process of change in ponding water depth can be coupled with the actual infiltration rate for calculation. The specific algorithmic flow for this boundary improvement is illustrated in Fig. 3.

(1) Firstly, at the start of each time step, determine the magnitude of pore water pressure at each node on the slope surface.

(2) Afterward, calculate the value of $I$ for each node on the slope surface based on Eq. (15). Positive values of $I$ indicate rainwater infiltration, while negative values indicate exfiltration. Then, use $I$ as the boundary condition for the Richard's equation and as the source-sink term for the runoff equation. Meanwhile, solve the two coupled equations for this time step to update the water depth and pore pressure on the slope surface for each subsequent time step.

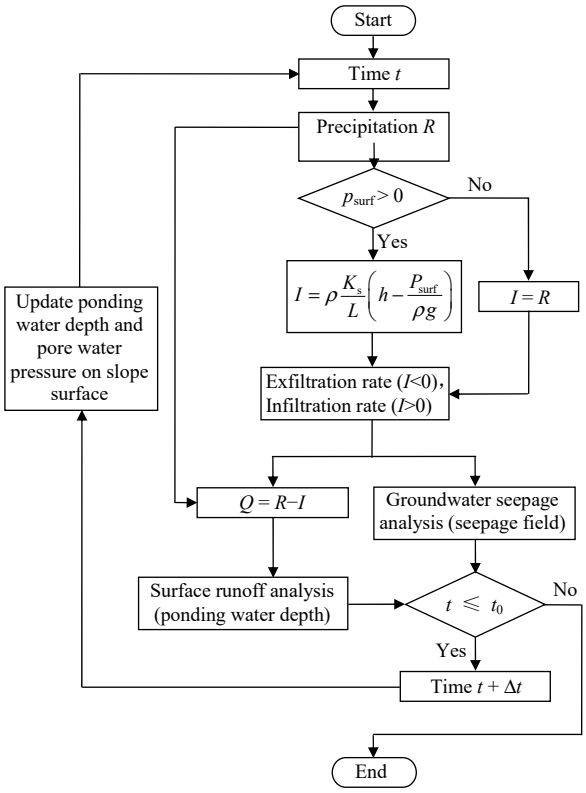


**Fig. 3 Improved flow chart of rainwater infiltration boundary based on diffusion wave approximation equation**

(3) Finally, determine if it is possible to proceed with the calculation for the next time step. If the computation duration exceeds the specified time limit $t_0$, exit the loop. If it does not exceed, proceed with the calculation for the next time step until the computation duration reaches the specified time limit.

From Fig. 3, it can be observed that the key to the transition from a pressure head boundary to a flux boundary using the improved rainfall boundary at the final stage of rainfall is the decreasing water depth calculated by Eq. (10) as the rainfall intensity decreases. Consequently, this results in a reduction in the soil surface infiltration rate calculated by Eq. (14). This reduced rainwater infiltration subsequently causes a decrease in soil surface pore pressure. Once the pore pressure at the soil surface becomes negative, the boundary condition shifts automatically from a pressure head boundary to a flux boundary controlled by rainfall intensity.

## 4 Validation of improved rainfall boundary

### 4.1 Verification with Lima test[10]

The first experimental study conducted by Lima[10] is utilized in this research to validate the accuracy of the improved rainfall boundary. The model used has dimensions

of 1 m in length, 0.5 m in width, and 0.8 m in depth, with a slope ratio of 10%. The soil used for the slope was sampled from Limburg, and the specific calculation parameters are listed in Table 1. In the experimental setup, the rainfall intensity was set at 0.037 41 mm /s, with a total duration of 15 min. After 15 min, the rainfall stopped, representing the stage of surface water recession. In the numerical model, the boundary conditions are set as follows: no-flow boundaries on the left, right and bottom sides of the model, an improved rainfall boundary on the slope surface, and a free-flow boundary at the toe of the slope (Fig. 4).

**Table 1 Relevant hydraulic parameters for calculation**

| Initial pore water head $H_{initial}$ /m | $R$ /(mm • s$^{-1}$) | $K_s$ /(m • s$^{-1}$) | $\theta_s$ | $\theta_r$ | $\alpha$ /m$^{-1}$ | $n$ | $n_m$ /(s • m$^{-\frac{1}{3}}$) |
|---|---|---|---|---|---|---|---|
| −1.2 | 0.037 41 | $1.67\times10^{-6}$ | 0.506 | 0.010 7 | 2.49 | 1.507 | 0.02 |

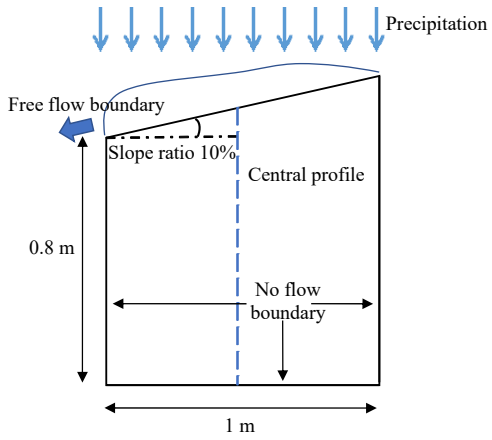


**Fig. 4 Schematic diagram of model test in Lima[10]**

From Fig. 5(a), it can be observed that the calculated unit width flow rate at the slope toe using the improved rainfall boundary in this study matches well with the results obtained from previous studies[10, 17−18]. Analysis of the curves reveals the following patterns: the initial runoff generation time obtained from the numerical modeling is earlier than the measured data. This discrepancy is attributed to the neglect of the gas phase in the pores in the Richard's equation used to describe unsaturated flow, while in reality, the presence of air in the soil slows down the infiltration process[15]. At the middle stage of the rainfall, once the runoff at the toe stabilizes, the calculated results with the improved rainfall boundary well agree with the results reported in the literature. At the final stage of rainfall, the calculated results with the improved boundary show better agreement with the measured data compared to other numerical results reported in the literature. Since the water depth of surface runoff on the slope is typically in the millimeter range or even smaller[18], it is challenging to measure directly through experiments. To validate the

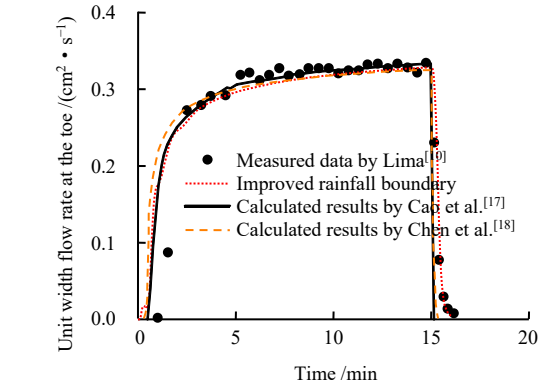


(a) Unit width flow rate at slope toe

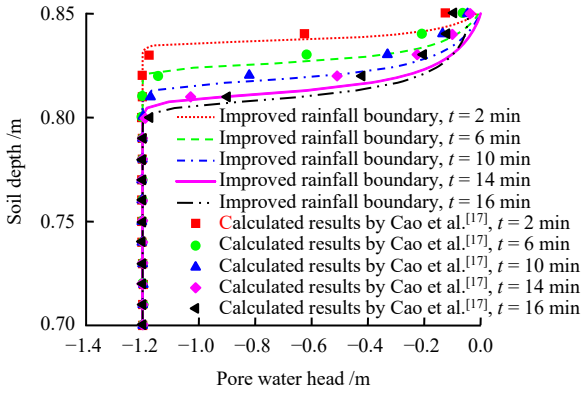


(b) Pore water head of soil in central profile of the slope

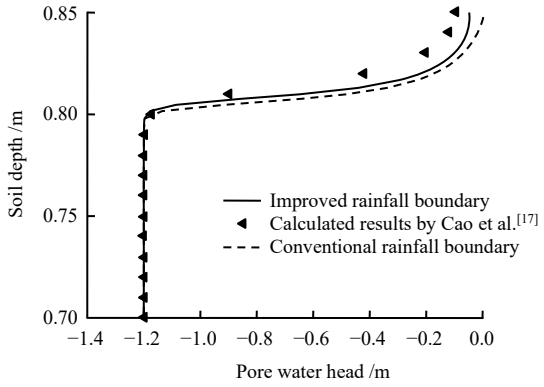


(c) Comparisons between improved and conventional rainfall boundaries at $t$ = 16 min

**Fig. 5 Comparisons of simulation results with literature**

accuracy of the calculated ponding water depth on the slope surface using the improved boundary, the calculated surface flow rates are compared with the results obtained from other studies. As the surface flow rates are calculated based on Eq. (9) (which indicates that the flow rate at a given location is uniquely determined by the ponding water depth), it can be observed from Fig. 5(a) that the calculated surface flow rates using the improved boundary are in a good agreement with the numerical results reported in other studies. This indirectly suggests that the calculated ponding water depths using the improved boundary are accurate. To verify the accuracy of the calculated seepage field using the improved rainfall boundary, Fig. 5(b) shows the variation of soil pore pressure head along the elevation

in the central profile of the slope model. The comparison is made between the results obtained using the improved rainfall boundary and the calculated results by Cao et al.[17]. It can be observed that the calculated results with the improved rainfall boundary exhibit a high degree of agreement with the calculated results reported by Cao et al.[17]. Figure 5(c) illustrates the comparison between the calculated results using the improved rainfall boundary and the conventional rainfall boundary at $t$ = 16 min during the surface water recession phase. The analysis focuses on this time point as there is no significant difference in the calculated results during the surface runoff generation phase. During the surface water recession process, the conventional rainfall boundary, as a steady-state pressure head boundary, fails to accurately capture the boundary transition at the final stage of rainfall. As a result, it overestimates the infiltration rate, leading to a larger error in the calculated pore pressure at the top of the slope compared to the results obtained using the improved rainfall boundary.

In conclusion, the improved rainfall boundary can provide a further basis for simulating the hydrological processes of rainwater infiltration and runoff on the slope surface.

### 4.2 Verification with Abdul et al. test[11]

The second case utilized in this study to validate the accuracy of the improved boundary is based on the model test conducted by Abdul et al.[11]. The model dimensions are 140 cm in length, 8 cm in width, and 120 cm in height, with the free water level located at the slope toe, approximately 76 cm above the ground. The slope ratio is 12°. The soil used for the slope is medium-dense sand, and the specific calculation parameters are listed in Table 2. The thickness of the capillary saturation zone for this soil is approximately 0.3 m, indicating that the model is in a saturated state[15]. The entire experiment lasts for 25 min, with the initial 20 min experiencing a rainfall intensity of $1.2\times10^{-5}$ m /s, representing the surface runoff generation phase. This is followed by a 5-min period of no rainfall, representing the surface water recession phase. In the numerical model, the boundary conditions are set as follows: no-flow boundaries on the left, right, and bottom sides of the model, an improved rainfall boundary on the slope surface, and a free-flow boundary at the slope toe (Fig. 6).

**Table 2 Relevant hydraulic parameters for calculation**

| $R$ /(m • s$^{-1}$) | $K_s$ /(m • s$^{-1}$) | Porosity $n_0$ | $\alpha$ /m$^{-1}$ | $n$ | $n_m$ /(s • m$^{-\frac{1}{3}}$) |
|---|---|---|---|---|---|
| $1.2\times10^{-5}$ | $3.5\times10^{-5}$ | 0.34 | 2.3 | 5.5 | 0.185 |

Figure 7 compares the calculated results using the improved rainfall boundary with the numerical results

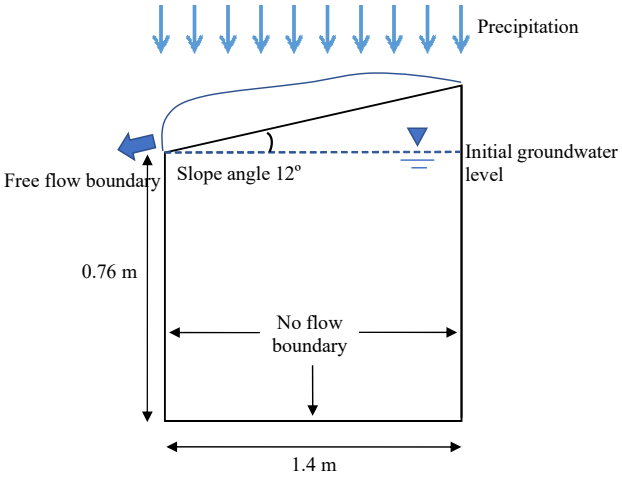


**Fig. 6 Diagram of model test in Abdul et al.[11]**

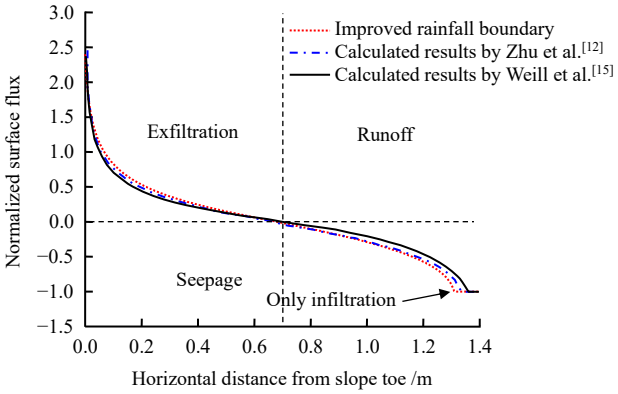


(a) Comparisons of calculated results of normalized flux along the surface at 19 min after rainfall

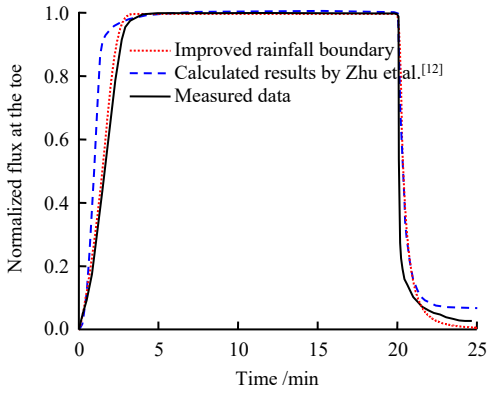


(b) Comparisons of calculated results and measured data of normalized flux at slope toe

**Fig. 7 Comparisons of simulation results with literature**

obtained from the literature[12, 15] and the measured data[11, 15]. It is evident that the calculated results with the improved rainfall boundary are rather accurate. Figure 7(a) shows the accuracy with which the improved rainfall boundary is able to simulate the rainwater infiltration, runoff, and seepage processes throughout a rainfall event. In a small section at the peak of the slope (where the normalized flux is −1), the rainwater is entirely absorbed. In the upper part of the slope (specifically the areas more than 0.7 m from the slope toe), rainwater partially infiltrates, with

the remainder forming surface accumulation and runoff. In the lower part of the slope, there is observable groundwater emergence. Figure 7(b) shows a satisfactory agreement between the normalized flux at the slope toe as calculated by the improved rainfall boundary, the measured data, and the computational outcomes from the numerical modeling in Zhu et al.[12]. This correlation indirectly substantiates the accuracy of the runoff depth calculation derived from the improved rainfall boundary.

In summary, the calculated results from these two classical experiments demonstrate that the improved rainfall boundary can accurately reflect the variation in slope runoff depth as well as the rainwater infiltration process. Therefore, it can adequately cater to the simulation of rainwater infiltration under complex rainfall conditions.

## 5 Analysis of engineering feasibility

### 5.1 Model conceptualization and numerical modeling

To assess the engineering feasibility of the improved rainfall boundary proposed in this paper, the central profile of a soil slope located in the Liangzhu Ancient City site in Hangzhou is chosen for rainwater infiltration calculation. The profile of the soil slope measures 11 m in length and 7 m in height, with the lower wall surface *BC* exhibiting a steep inclination ranging from 55º to 70º, as illustrated in Fig. 8(a). Considering the weathering- and water infiltration-induced damage experienced by the lower part of the slope, the site management committee has implemented a rain shelter to protect the lower slope wall. Subsequent drilling and sampling conducted on the site revealed that the predominant composition of the soil slope is silty clay (soil parameters obtained from the laboratory tests are listed in Table 3). Notably, the deepest occurrence of bedrock is found in the central portion of the slope, with an approximate depth of 15 m (the influence of bedrock has been disregarded during the modeling process).

**Table 3 Relevant hydraulic parameters for calculation**

| Dry density $\rho_s$ /(kg • m$^{-3}$) | $K_s$ /(m • s$^{-1}$) | $\theta_s$ | $\theta_r$ | $\alpha$/cm$^{-1}$ | $n$ | $n_m$ /(s • m$^{-\frac{1}{3}}$) |
|---|---|---|---|---|---|---|
| 1 600 | 1×10$^{-7}$ | 0.4 | 0.071 3 | 0.006 3 | 1.589 8 | 0.55 |

Considering the actual site conditions, the boundary conditions for the soil slope in the archaeological site are specified as follows: *AD* and *CD* are set as no flux boundaries, *BC* is designated as a free seepage boundary, and *AB* is considered a rainfall boundary based on the diffusion wave approximation equation. When the diffusion wave approximation equation is applied, the boundary conditions at the two endpoints of the slope *AB* are defined as follows: Point *A* is set as a no-flow boundary, while point *B* is assigned as a free-flow boundary. According to the drilling data, the groundwater level is approximately at an elevation of 1 m. To improve the calculation accuracy, mesh refinement is conducted for slope *AB* due to the rapid changes in surface pressure during rainfall events. Figure 8(b) shows the computational model, which contains a total of 3 758 triangular meshes.

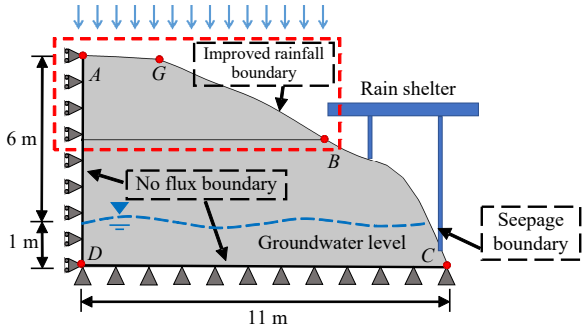


(a) Model diagram

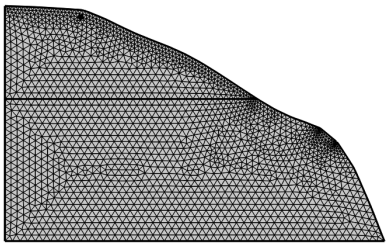

(b) Mesh generation

**Fig. 8 Illustrations of central profile of an earthen archaeological site**

The archaeological site is situated within the Tianmu Mountain range, which is the largest rainstorm center in Zhejiang Province, China. The surface runoff in the region primarily originates from precipitation. In this study, rainfall data from the 2019 “Lekima” typhoon weather event[19] are selected. The maximum rainfall intensity is set to 290 mm /d, with a duration of 20 h. To assess the effectiveness of the proposed improvement to the rainfall boundary, a concentrated rainfall sequence is assumed, as shown in Fig. 9.

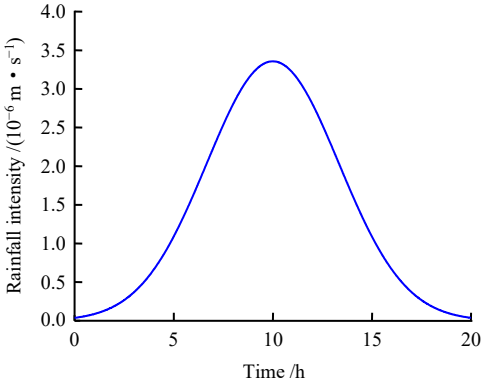


**Fig. 9 Time series of concentrated rainfall**

### 5.2 Results and discussion

In this section, we compare the application of the improved rainfall boundary with the conventional one for the calculation of rainwater infiltration on the soil slope of the archaeological site. We discuss the evolution of the average infiltration rate, average pore pressure, total infiltration volume, and average water depth on the slope surface to assess the engineering feasibility of the improved rainfall boundary.

Figure 10(a) shows the temporal variation of the average rainwater infiltration rate on the slope *AB*. Under the concentrated rainfall conditions, when the conventional rainfall boundary is implemented, the slope *AB* experiences a unidirectional transition from the flux boundary to the pressure head boundary. At the final stage of rainfall, the calculated infiltration rate on the slope exceeds the rainfall intensity, which contradicts the principle of mass conservation[4]. In contrast, when the improved rainfall boundary is used, the slope *AB* undergoes a dynamic, bidirectional transition involving the flux boundary, pressure head boundary, and then back to the flux boundary. At the early stage of rainfall, the infiltration capacity of the soil equals the rainfall intensity, and the rainwater fully infiltrates, forming a flux boundary. At the middle stage of rainfall, the soil surface becomes saturated. The rainfall intensity exceeds the infiltration capacity of the soil surface, leading to the formation of surface runoff that flows along the slope. Additionally, a portion of the rainwater infiltrates the soil (controlled by the runoff depth, creating pressured infiltration), establishing a pressure head boundary. At the final stage of rainfall, as the rainfall intensity reduces, the actual infiltration rate depends on the rainfall intensity, resulting in the transition of the rainfall boundary back to a flux boundary.

Figure 10(b) shows the temporal changes of average pore pressure on the slope *AB*. Under the concentrated rainfall conditions, when the conventional rainfall boundary is employed, the average pore pressure on the slope gradually rises at the initial stages of rainfall, and stabilizes thereafter until the rainfall cessation. In contrast, when the improved rainfall boundary is used, the variation trends of the pore water pressure at the early and middle stages of rainfall agree with those resulting from the conventional rainfall boundary. However, at the final stage of rainfall, as the rainfall intensity decreases, it is deduced from Eq. (15) that the rate of rainwater infiltration on the slope reduces. This decrease in turn leads to a reduction in the slope's pore pressure and a state of non-saturation, thereby transitioning the rainfall boundary from the pressure head boundary back to the flux boundary. This also highlights the inherent limitations of the conventional rainfall boundary,

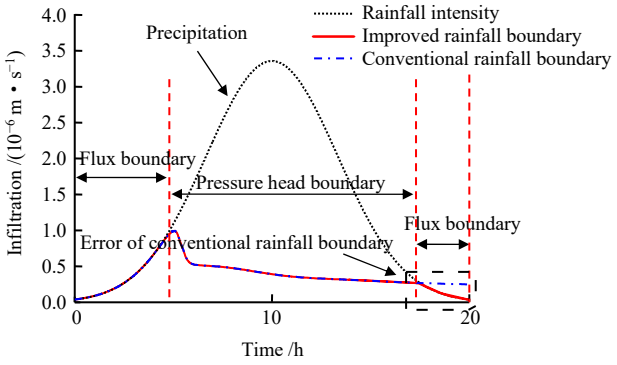


(a) Variations of average infiltration rate

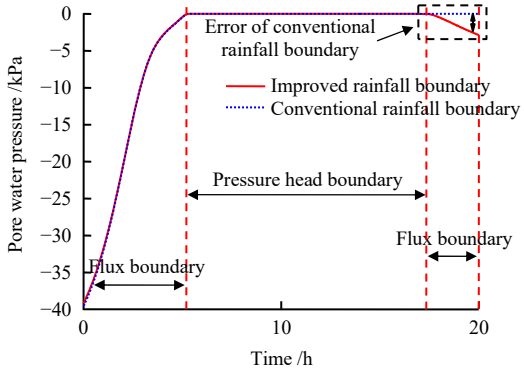


(b) Variations of average pore water pressure

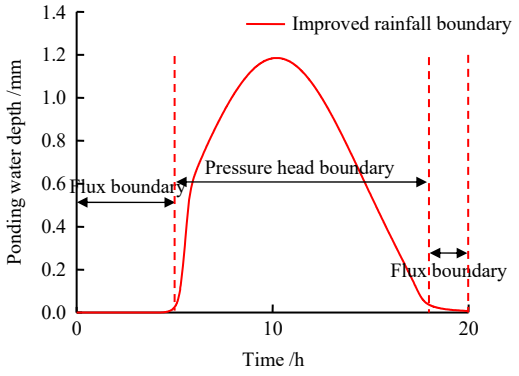


(c) Average ponding water depth calculated by improved rainfall boundary

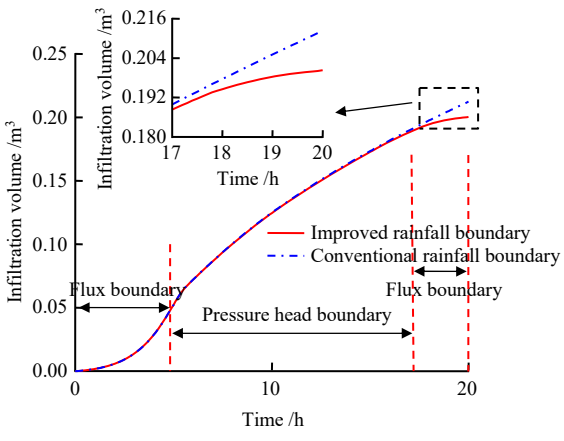


(d) Variations of infiltration volume

**Fig. 10 Comparisons between calculated results of improved and conventional rainfall boundaries**

which presumes a static, constant ponding water depth on the slope during saturation. This assumption is inadequate in effectively facilitating a real-time dynamic transition of boundary condition.

Figure 10(c) illustrates the temporal evolution of the average depth of accumulated water on the slope *AB*. Within the framework of the conventional rainfall boundary, the average ponding water depth can be considered equivalent to the mean water depth as calculated by the improved rainfall boundary, i.e. $9.1\times10^{-4}$ m. When the improved rainfall boundary is applied, at the initial stage of rainfall, the rainfall intensity equals the infiltration rate, leading to complete absorption of the rainwater and the absence of slope runoff. As the rainfall transitions into its middle stage, the slope surface becomes saturated, leading to partial infiltration of rainwater and the onset of slope runoff. From 0 h to 10 h, an increase in rainfall intensity results in a corresponding gradual increase in average runoff depth. Conversely, after 10 h, a decrease in rainfall intensity brings about a gradual reduction in average runoff depth. At the final stage of rainfall, when the flux boundary is used, the rainfall intensity decreases to a point below the maximum infiltration capacity of the slope, leading to complete infiltration of the rainwater. At this stage, the runoff depth becomes negligible. It is thus evident that the progression of average ponding water depth on the slope, as calculated by the improved boundary, is consistent with the natural laws.

Figure 10(d) shows the variation of the total infiltration volume over time on the slope *AB*. At the initial stage of rainfall, the rainfall boundary is characterized as a flux boundary, and the growth rate of infiltration volume progressively increases with the increase in rainfall intensity. As the rainfall transitions into middle stage, the flux boundary evolves into a pressure head boundary, which results in the stabilization of the growth rate of infiltration volume. At the final stage of rainfall, the total infiltration volume derived from the improved rainfall boundary proves to be less than that calculated from the conventional rainfall boundary. This outcome can be attributed to that when the improved rainfall boundary is employed, the pressure head boundary transitions back to the flux boundary as the rainfall intensity decreases. In contrast, since the ponding water depth after slope soil saturation is assumed to be constant, the conventional rainfall boundary tends to overestimate the rainwater infiltration volume at the final stages of rainfall.

Figure 11 shows the dynamic evolution processes of the ponding water depth distribution on the slope at different times, i.e. 5, 10, 15, and 20 h. According to Fig. 10, at 5 h, which marks the initial transition from the flux boundary to the pressure head boundary, there is almost no runoff generated on the slope. The deepest ponding water is observed at the slope toe, measuring $1.9\times10^{-4}$ m. At 10 h, the rainfall intensity reaches its peak, resulting in a maximum average water depth on the slope, with the deepest ponding water depth observed at the slope toe, measuring $1.8\times10^{-3}$ m. At 15 h, as the rainfall intensity gradually decreases, the ponding water depth on the slope decreases correspondingly. The deepest ponding water is still located at the slope toe, with a depth

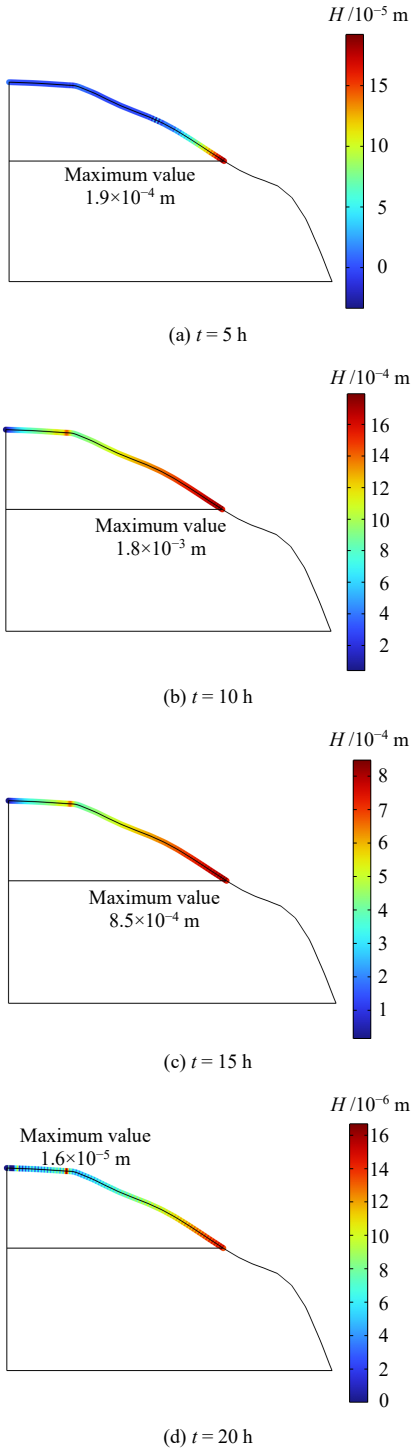


**Fig. 11 Distributions of ponding water depth on slope surface at different moments**

of $8.5\times10^{-4}$ m. Figure 11(a)−(c) illustrates that at the initial, middle and final stages of the pressure head boundary at the slope surface *AB*, the theoretically calculated maximum ponding water depth is located at the slope toe. This phenomenon results from runoff flowing freely from the top to the base of the slope and accumulating at the toe. At 20 h, with the decrease in rainfall intensity and the transition of rainfall boundary to a flux boundary, the depth of the surface runoff can be disregarded. In theory, the point of deepest ponding water, as calculated by the improved rainfall boundary, appears at the intersection of the flat slope surface *AG* and the steep slope surface *BG*. This is probably due to that the residual water on the slope does not possess the energy to overcome the slope's resistance to flow into the steep slope *BG*, thus causing it to stagnate at point *G*, the terminal point of the flat slope surface.

## 6 Conclusions

In this study, the conventional rainfall boundary is improved based on the diffusion wave approximation equation, allowing for the coupled calculation of dynamic changes in ponding water depth on the slope and rainwater infiltration. The accuracy of the improved rainfall boundary is verified through two classical case studies. Furthermore, the improved rainfall boundary is applied to analyze actual engineering cases. The following conclusions are drawn:

(1) The improved rainfall boundary allows for real-time dynamic transition between flux boundary and pressure head boundary under concentrated rainfall conditions, overcoming the limitation of conventional rainfall boundaries that only allow one-way transition from flux boundary to pressure head boundary.

(2) The improved rainfall boundary facilitates the coupled computation of ponding water depth on the slope and the actual rainwater infiltration process, and accurately captures the variation pattern of ponding water depth and its impact on the rainwater infiltration rate.

(3) The case studies show that under the pressure head boundary, the point of maximum ponding water depth on the slope theoretically occurs at the slope toe. Conversely, under the flux boundary, the theoretical maximum ponding water depth is found at the intersection of flat and steep slope surfaces at the final stage of rainfall.

### References

[1] XU Quan, TAN Xiao-hui, SHEN Meng-fen. Stability analysis of soil slopes under rainfall infiltration[J]. Chinese Journal of Geotechnical Engineering, 2012, 34(Suppl.1): 254−259.

[2] WANG Hua-bin, LI Jian-mei, JIN Yi-xuan, et al. The numerical methods for two key problems in rainfall-induced slope failure[J]. Rock and Soil Mechanics, 2019, 40(2): 777−784.

[3] NG CHARLES W W, CHEN Shou-yi, PANG Yu-wei. Parametric study of effects of rainfall infiltration on unsaturated slopes[J]. Rock and Soil Mechanics, 1999, 20(1): 1−14.

[4] NIAN Geng-qian, CHEN Zhong-hui, ZHANG Liang-fan, et al. Treatment of two boundary conditions for rainfall infiltration in slope and its application[J]. Rock and Soil Mechanics, 2020, 41(12): 4105−4115.

[5] LOU Yi-qing. Finite element analysis of slope seepage and stability due to rainfall infiltration[J]. Journal of Hydraulic Engineering, 2007(Suppl.1): 346−351.

[6] MAY CHUI T F, FREYBERG D L. Implementing hydrologic boundary conditions in a multiphysics model[J]. Journal of Hydrologic Engineering, 2009, 14(12): 1374−1377.

[7] HOU Xiao-ping, FAN Heng-hui. Study on rainfall infiltration characteristics of unsaturated fractured soil based on COMSOL Multiphysics[J]. Rock and Soil Mechanics, 2022, 43(2): 563−572.

[8] DOU Zhi, LIU Yi-min, ZHOU Zhi-fang, et al. Improvement of rainfall boundary treatment based on single and double permeable media[J]. Rock and Soil Mechanics, 2022, 43(3): 789−798.

[9] CHIU Y, CHEN H, YEH K. Investigation of the influence of rainfall runoff on shallow landslides in unsaturated soil using a mathematical model[J]. Water, 2019, 11(6): 1178.

[10] LIMA J L M P. Model KINNIF for overland flow on pervious surfaces[C]//Overland Flow: Hydraulics and Erosion Mechanics. London: UCL Press, 1992: 69−88.

[11] ABDUL A S, GILLHAM R W. Laboratory studies of the effects of the capillary fringe on streamflow generation[J]. Water Resources Research, 1984, 20(6): 691−698.

[12] ZHU Y, ISHIKAWA T, SIVA SUBRAMANIAN S, et al. Simultaneous analysis of slope instabilities on a small catchment-scale using coupled surface and subsurface flows[J]. Engineering Geology, 2020, 275: 105750.

[13] VAN GENUCHTEN M T. A closed-form equation for predicting the hydraulic conductivity of unsaturated soils[J]. Soil Science Society of American Journal, 1980, 44(5): 892-898.

[14] MUALEM Y. A new model for predicting the hydraulic conductivity of unsaturated porous media[J]. Water Resources Research, 1976, 12(3): 513−522.

[15] WEILL S, MOUCHE E, PATIN J. A generalized Richard's equation for surface/subsurface flow modeling[J]. Journal of Hydrology, 2009, 366(1-4): 9−20.

[16] TIAN D, LIU D. A new integrated surface and subsurface flows model and its verification[J]. Applied Mathematical Modelling, 2011, 35(7): 3574−3586.

[17] CAO Zhi-xian, ZHANG Can-heng, WANG Xin. Coupled hydrodynamic modeling of surface runoff and underground seepage[J]. Engineering Journal of Wuhan University, 2010, 43(5): 545−548.

[18] CHEN Li, LIU Qing-quan, LI Jia-chun. Study on the runoff generation process on the slope with numerical method[J]. Journal of Sediment Research, 2001(4): 61−67.

[19] DONG Mei, GUO Qing-ling, KONG Meng-yue, et al. Slope stability analysis of Laohuling site in Archaeological Ruins of Liangzhu city considering real rainfall conditions[J]. Journal of Ground Improvement, 2021, 3(3): 231−237.